



## **Dynamic Stability of Deep and Slender Wide-Flange Steel Columns – Full Scale Experiments**

Ahmed Elkady<sup>1</sup>, Dimitrios G. Lignos<sup>2</sup>

### **Abstract**

In North America, a common design practice for steel frame buildings with perimeter steel special moment frames (SMFs) is to employ deep and slender wide-flange steel columns (i.e., range of column depth,  $d > 16$  inches). Till recently, very little was known regarding the hysteretic behavior of such members because of lack of available experimental data. This paper discusses selective findings from a full-scale testing program that was conducted at École Polytechnique Montréal with the use of a 6-degree-of-freedom experimental setup. The testing program investigated the cyclic behavior of 10 full-scale beam-columns. The specimens had a depth of 24 inches (i.e., W24x146 and W24x84 cross-sections) and were subjected under various lateral-loading protocols coupled with constant compressive axial load. The boundary conditions of the specimens simulated a fixed support at the column base and a flexible boundary at the column top end to mimic the flexibility of a beam-to-column connection at the floor level. The tested specimens represented typical interior first-story columns in mid-rise steel SMFs. This paper summarizes the main observations related to the effect of local and global slenderness ratios on the cyclic behavior of beam-columns. The effect of bidirectional lateral loading on the dynamic stability of beam-columns is also addressed. Observations related to the effect of the employed loading history as well as the lateral bracing force design requirements on steel wide-flange beam-columns are also provided based on the available experimental results.

### **1. Introduction**

In North America, a common design practice is to concentrate the lateral force-resisting system in the perimeter of steel frame buildings. In this case, special moment frames (SMFs) as per ANSI/AISC-341-10 (AISC 2010a) typically utilize deep beams to control the lateral story drift-ratio limits specified by the regional seismic design-code provisions (ASCE 2010). As a result, designers tend to use deep and slender steel wide-flange columns in order to satisfy the strong-column-weak-beam criterion. Deep and slender wide-flange cross-sections provide the required large moment-of-inertia while respecting the economy due to their low weight. The term “deep” refers to wide-flange cross-sections with a depth larger than 16 inches. The web and flange local slenderness ratios of these cross-sections satisfy the compactness limits for highly ductile members based on AISC (2010a). Finite element studies on deep and slender steel wide-flange

---

<sup>1</sup> Ph.D. Candidate, McGill University, <ahmed.elkady@mail.mcgill.ca>

<sup>2</sup> Associate Professor, École Polytechnique Fédérale de Lausanne, <dimitrios.lignos@epfl.ch>

beam-columns (Newell and Uang 2006; Elkady and Lignos 2012, 2013, 2015a; Fogarty and El-Tawil 2015) suggest that these members may deteriorate rapidly in flexural strength and stiffness due to local and global geometric instabilities. Summaries from past experimental studies of deep and slender wide-flange steel beams (FEMA 2000; Lignos and Krawinkler 2011, 2013) indicate that such members deteriorate rapidly due to local and out-of-plane geometric instabilities at fairly small lateral deformations. Furthermore, Zhang and Ricles (2006) demonstrated experimentally that deep and slender wide-flange columns as part of fully restrained beam-to-column connections are susceptible to twisting once local buckling occurs in the respective steel beam. However, these columns were not subjected to compressive loads.

Till recently, experimental data related to the hysteretic behavior of deep and slender steel wide-flange beam-columns, under lateral drift demands coupled with axial load was not available. The main reason was the associated laboratory equipment limitations to test such members at full-scale. Therefore, a number of design provisions related to their seismic design as per AISC (2010b) should be carefully examined. NIST (2010) established a research plan that highlighted the need for further research related to the hysteretic behavior of deep wide-flange beam-columns as part of steel moment-resisting frames (MRFs) under earthquake loading. To this end, certain aspects of their behavior were characterized experimentally by Uang et al. (2015). However, issues related to the effect of the employed loading history, the boundary conditions at the ends of the member and the bidirectional loading was not addressed. Another issue that was not addressed was how large the out-of-plane forces that typically act on the lateral brace of a column at the floor level. This is particularly important once local and global instabilities occur. In order to address the aforementioned issues, a testing program was carefully designed and executed at full-scale that investigated the cyclic behavior of ten deep and slender steel wide-flange beam-columns.

## 2. Test Setup

The testing program was conducted using the 6 degree-of-freedom (6-DOF) test setup at the structures laboratory of École Polytechnique de Montréal. Fig.1 shows the test-setup that was developed by MTS Corporation. The 6-DOF control-system comprises of a steel base plate anchored to the laboratory's strong floor and a steel top platen connected to a total of eight actuators; four vertical and two horizontal actuators per loading direction as shown in Fig. 1. The eight actuators provide full control of the 6-DOF ( $x$ ,  $y$ ,  $z$ ,  $x$ ,  $y$ ,  $z$ ) at the top platen with mixed displacement/force control mode. Each one of the four vertical actuators has a force capacity of  $\pm 405$  kips and a displacement stroke of  $\pm 12$  inches. Each one of the four horizontal actuators has a force capacity of  $\pm 225$  kips and a displacement stroke of  $\pm 15$  in. This system automatically tracks the 6-DOF deformations and the corresponding forces at the top platen during a test. The 6-DOF system makes it possible to test at full-scale steel beam-columns under unidirectional and bidirectional cyclic lateral loading coupled with axial force. Furthermore, by applying rotation at the top platen, this system is able to realistically simulate the effect of boundary conditions on the hysteretic behavior of steel beam-columns. In particular, the flexibility of a beam-to-column connection at the top of a steel beam-column can be considered as part of a test. This allows for testing of beam-columns without considering a fixed point of inflection along the height of the member, if necessary. It should be noted that the effect of boundary conditions on the beam-column performance has never been investigated in prior experimental studies. Fig. 2a illustrates schematically the deformed configuration of a beam-

column with fixed boundary conditions at its ends. Similarly, Fig.2b illustrates how the same beam-column deforms laterally when the flexibility of the beam-to-column connection is considered. In this case, the location of the inflection point is not fixed. Instead, it moves while plastification progresses in the beam-column due to force redistributions.

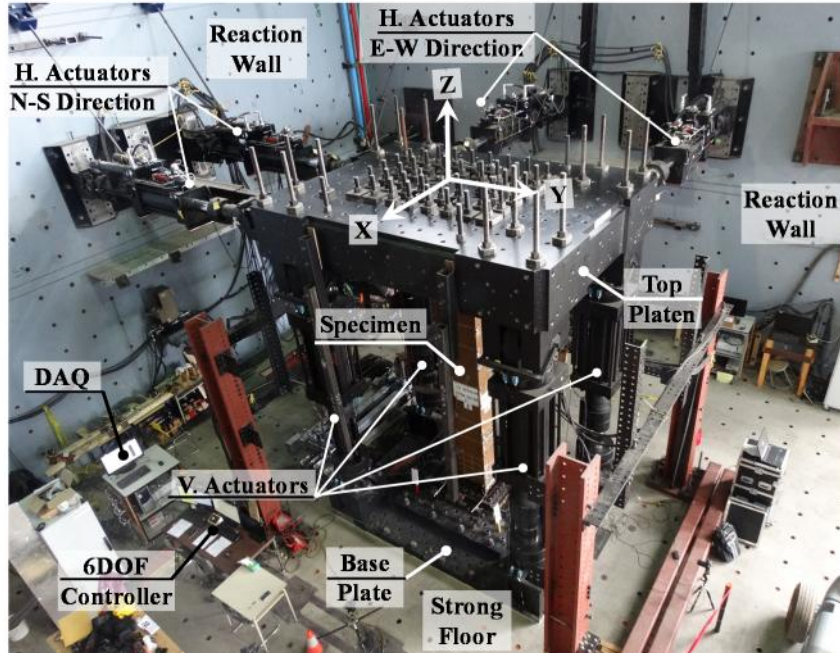


Figure 1: Overview of the 6-DOF setup at École Polytechnique de Montréal

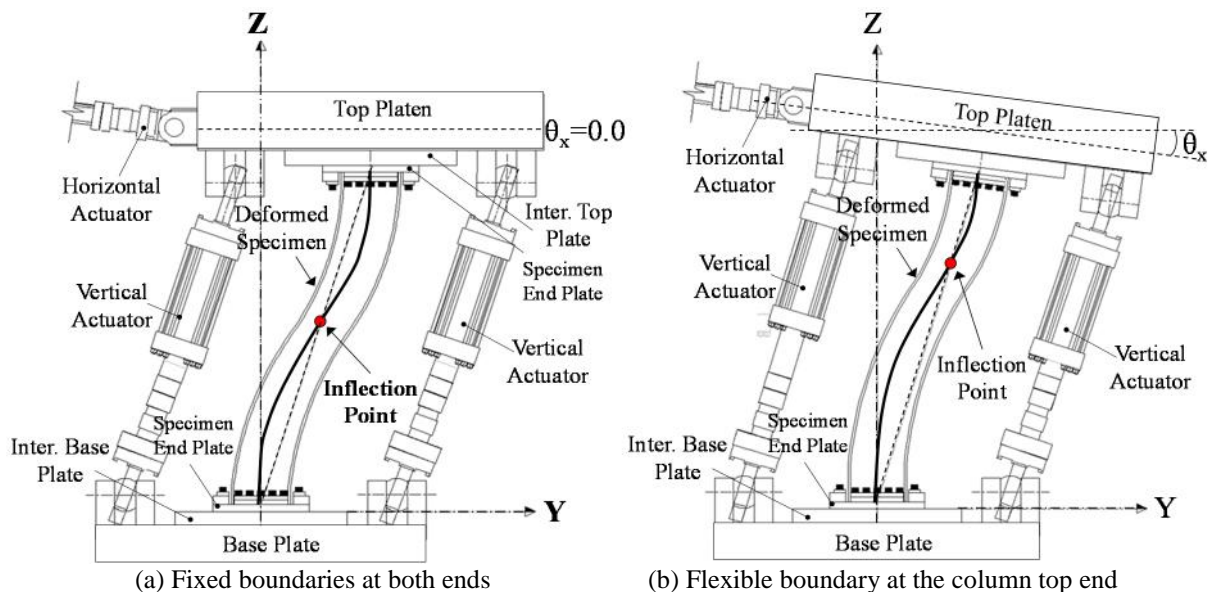


Figure 2: Deformation configuration of a beam-column with different boundary conditions

### 3. Test Matrix and Specimens

Beam-columns with W24 cross-sections were considered for experimental testing at full-scale. This cross-section size is commonly used in steel SMFs according to today's practice (Elkady and Lignos 2014, 2015b) In particular, two wide-flange cross-sections, W24x146 and W24x84,

were selected after a preliminary finite element study by Elkady and Lignos (2015a) that investigated what the critical parameters are that influence the hysteretic behavior of deep and slender steel wide-flange beam-columns. Table 1 summarizes the geometric, axial and flexural strength properties of the selected cross-sections (assuming an expected yield stress,  $F_y=55\text{ksi}$ ). Fig. 3 shows all the W24 cross-sections, available in the AISC database. These cross-sections are plotted in terms of their web ( $h/t_w$ ) versus flange slenderness, ratio ( $b_f/2t_f$ ). The AISC (2010a) web and flange compactness limits for highly ductile members ( $\lambda_{hd}$ ) are superimposed in the same figure. For an axial load ratio  $P/P_y=0.2$  (in which,  $P_y$  is the axial yield strength), the flange and web compactness limits for highly ductile members are 7 and 47.8, respectively. The web compactness limit for  $P/P_y=0.5$  is also superimposed in the same figure for reference. Based on Table 1 and Fig. 3, the web and flange compactness ratios of these cross-sections comply with the compactness limits for highly ductile members as per AISC (2010a), given an axial load level of 20%  $P_y$ . The two selected cross-sections have about the same  $b_f/2t_f$  ratio but different  $h/t_w$  ratios. This parameter seems to significantly affect the hysteretic behavior of steel beam-columns as discussed in MacRae et al. (1990).

Table 1: Geometric properties and expected axial and flexural strength of the W24x146 and W24x84 beam-columns

Column size	$\frac{h}{t_w}$	$\frac{b_f}{2t_f}$	$r_y$ [in]	$\frac{L_b}{r_y}$	$P_y$ [kips]	$M_p$ [kip.in]
W24x146	33.2	5.9	3.0	51	2365	22990
W24x84	45.9	5.9	1.9	79	1359	12320

The W24x84 column has a global slenderness ratio,  $L_b/r_y = 79$  (in which,  $L_b$  is the laterally unbraced length of the column and  $r_y$  is the weak-axis radius of gyration of the cross-section). The W24x146 cross-section has a  $L_b/r_y = 51$  as seen in Table 1. Note that  $L_b$  is equal to the clear length of the beam-column specimen ( $L$ ), which is 12.8 feet. Therefore, the effect of global slenderness on the column performance can be assessed. The AISC (2010a) seismic provisions do not specify a  $L_b/r_y$  limit for columns in steel SMFs when the beam-to-column connection is laterally braced [see Section 4c.1, AISC (2010a)]. However, the AISC (2010a) provisions specify a  $L/r_y$  limit of 60 only when the beam-to-column connections are not laterally braced (see [Section 4c.2, AISC (2010a)]). This can be the case in atriums and two-story warehouses. On the other hand, the Canadian seismic provisions CSA (2009) specify that  $L_b/r_y$  should be less than  $(17250+15500 \lambda)/F_{yn}$ , in which  $\lambda$  is the ratio of the smaller-to-larger moment at opposite ends of the beam-column's unbraced length and  $F_{yn}$  is the nominal yield stress of the steel material. Assuming that the beam-column is in single curvature (i.e.,  $\lambda=0$ )  $L_b/r_y$  should not exceed 50.

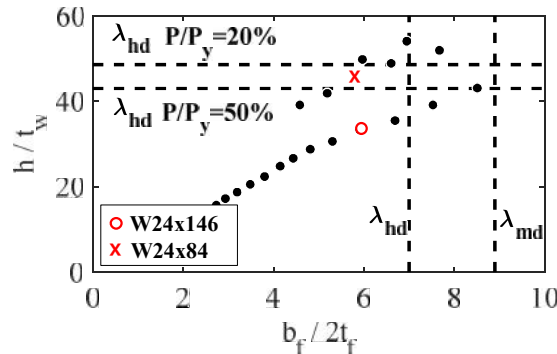


Figure 3: Distribution of web and flange slenderness for W24 steel beam-columns

The two selected cross-sections are incorporated in a test matrix that involves a total of ten specimens (labeled as C1 to C10). All ten specimens are fabricated from A992 Grade-50 steel material as per ASTM (2014) from two different heats. Table 2 provides an overview of the selected cross-sections, the employed lateral loading protocol, the applied compressive axial load ratios, and the boundary conditions at the beam-column ends in both loading directions for each specimen. In brief, the test matrix includes six nominally identical W24x146 specimens and four W24x84 specimens. Two types of lateral loading protocols are employed: a unidirectional and a bidirectional. Each protocol is further split into two additional categories: 1) a symmetric lateral loading protocol, and 2) a collapse-consistent lateral loading protocol. The second protocol represents seismic events with low probability of occurrence and reflects the ratcheting behavior that a frame building experiences prior to structural collapse (Lignos et al. 2011).

Table 2: Test matrix summary

Specimen ID	Section size	Lateral protocol	$\frac{P}{P_y}$	End boundary conditions	
				Strong-axis	Weak-axis
C1	W24x146	AISC-Symmetric (Unidirectional)	-0.2	Fixed- Fixed	Fixed-Fixed
C2	W24x146	AISC-Symmetric (Unidirectional)	-0.5	Fixed- Fixed	Fixed-Fixed
C3	W24x146	AISC-Symmetric (Unidirectional)	-0.2	Fixed-Flexible	Fixed-Fixed
C4	W24x146	Collapse-Consistent (Unidirectional)	-0.2	Fixed-Flexible	Fixed-Fixed
C5	W24x146	Collapse-Consistent (Unidirectional)	-0.2	Fixed-Flexible	Fixed-Fixed
C6	W24x146	AISC-Symmetric (Bidirectional)	-0.2	Fixed-Flexible	Fixed-Fixed
C7	W24x84	AISC-Symmetric (Unidirectional)	-0.2	Fixed-Flexible	Fixed-Fixed
C8	W24x84	Collapse-Consistent (Unidirectional)	-0.2	Fixed-Flexible	Fixed-Fixed
C9	W24x84	AISC-Symmetric (Bidirectional)	-0.2	Fixed-Flexible	Fixed-Fixed
C10	W24x84	Collapse-Consistent (Bidirectional)	-0.2	Fixed-Flexible	Fixed-Fixed

Fig. 4a shows the history of the unidirectional symmetric lateral loading protocol in terms of the beam-column chord-rotation in the YZ plane,  $\theta_{YZ}$  (see Fig. 1). This protocol is incorporated in AISC-341-10 (AISC 2010a) for the pre-qualification of fully-restrained beam-to-column moment connections (Clark et al. 1997). Fig. 4b shows the history of the unidirectional collapse-consistent loading protocol developed by Suzuki and Lignos (2015). This protocol is useful for the characterization of the hysteretic behavior of steel beam-columns at large displacements associated with structural collapse. Figs. 4c and 4d show the history of drift-ratio in the X-axis direction versus that in the Y-axis direction for a symmetric and a collapse-consistent bidirectional lateral loading protocol, respectively. These protocols were developed specifically for the testing program discussed in this paper through 3-dimensional nonlinear response-history analysis of a prototype four-story archetype steel frame building with perimeter SMFs. A set of 30 ground-motion records was used for this purpose. Note that the drift-ratio histories in the Y-direction for the symmetric and the collapse-consistent bidirectional protocols are consistent with those of the unidirectional symmetric and collapse-consistent protocols, respectively. This was intentionally targeted during the protocol development such that the effects of unidirectional and bidirectional loading on the beam-column performance could be assessed.

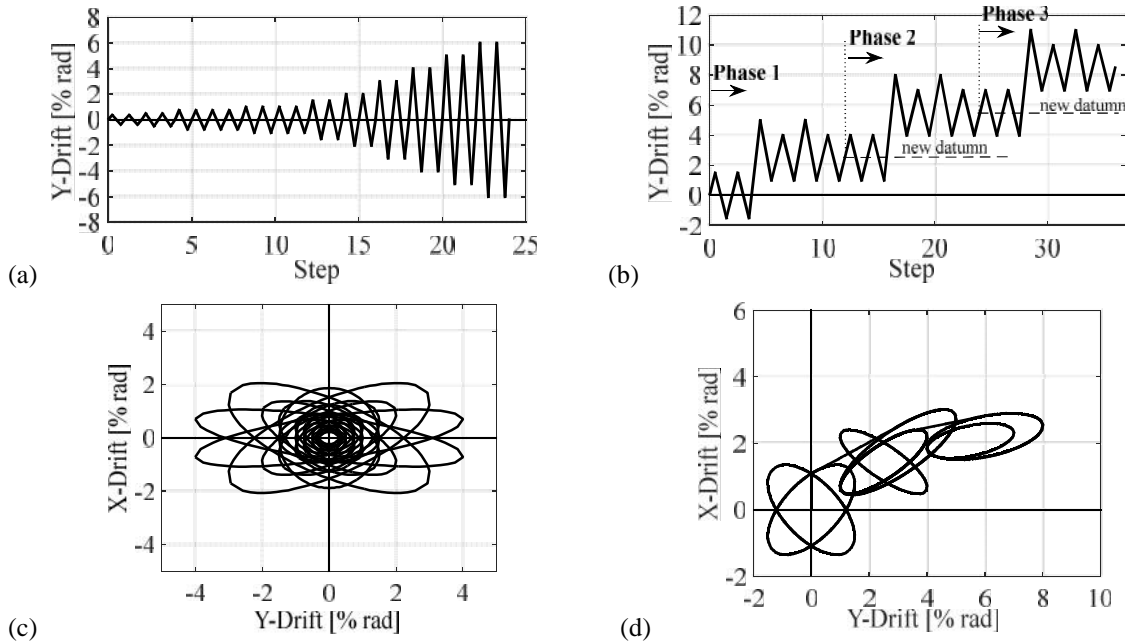


Figure 4: Lateral loading protocols utilized in the testing program: (a) unidirectional AISC-symmetric loading protocol (Clark et al. 1997); (b) unidirectional collapse-consistent loading protocol (Suzuki and Lignos 2014); (c) bidirectional symmetric loading protocol; (d) bidirectional collapse-consistent loading protocol

In summary, except for specimen C2, the rest of the test specimens were subjected to a constant compressive axial load ratio,  $P/P_y = 20\%$ . Specimen C2 was tested under a constant compressive axial load ratio  $P/P_y = 50\%$ . Specimens C1 and C2 were tested with fixed boundary conditions at both beam-column ends. For specimens C3 to C10, a pre-described rotation ( $\theta_x$ ) was applied at the beam-column top end. The rotation history was synchronized with the applied lateral drift in the strong-axis ( $y$ ), as illustrated in Fig. 2b. This was done to achieve a flexible boundary condition at the column top, in the strong-axis direction of the beam-column (noted as fixed-flexible). This is a realistic representation of the boundary conditions of first-story columns in steel MRFs due to the flexibility of the beam-to-column connection at the second floor. During the elastic loading range of the protocol, the pre-described rotation,  $\theta_x$  was such that the inflection point was located at a distance equal to  $0.75 L$  from the column base. A fixed-fixed boundary condition was employed in the weak-axis orientation of all ten specimens. This assumption is justified because in a steel frame building, the orthogonal gravity beam-to-column connection and the floor slab typically provide out-of-plane restraint at the beam-column top end.

Table 3 summarizes the mechanical properties of the employed cross-sections as measured from typical tensile coupon testing. The ten specimens were heavily instrumented. In total, 71 sensors are employed including 54 unidirectional strain gauges, displacement sensors as well as rotation sensors. A wireless tracking unit, with 24 sensors along the specimen height, was also employed to measure the deformation of a specimen in space. In addition, 6 out-of-plane string potentiometers were utilized to measure the out-of-plane deformations (i.e., in the X-axis direction) at three locations along the specimen height (at  $L/4$ ,  $L/2$  and  $3L/4$ ). The same string potentiometers were used to measure beam-column twisting.

Table 3: Measured material properties based on coupon tensile testing – values are based on 3 coupons per location

Heat no.	Section size	Location	E [ksi]	$F_y$ [ksi]	$F_u$ [ksi]	$\epsilon_y$ [%]	$\epsilon_u$ [%]	fracture [%]
1	W24x146 (C1 to C4)	web	27768	60.2	72.8	0.18	13.0	23.5
		flange	27486	60.0	73.8	0.17	12.7	26.3
2	W24x146 (C5 to C6)	web	29431	54.8	69.5	0.14	12.8	22.8
		flange	29864	53.4	70.1	0.16	13.2	26.1
2	W24x84 (C7 to C10)	web	27979	50.0	73.7	0.13	14.3	21.3
		flange	28645	48.2	73.5	0.17	14.3	22.3

#### 4. Experimental Results and Discussion

This section provides an indicative summary of the damage progression in two out-of-ten specimens that were tested due to brevity. A synthesis of the experimental results from all ten specimens is then provided that addresses the objectives of the experimental program that was outlined in the previous section of this paper. Specimen C6 (W24x146,  $P/P_y=0.2$ ) and C9 (W24x84,  $P/P_y=0.2$ ) are selected to illustrate the typical damage progression observed in the test series. Both specimens were subjected to a bidirectional symmetric lateral loading protocol and had flexible boundaries at their top end in the strong-axis orientation. Figs. 5 and 6 summarize the damage progression observed in both specimens. Each figure includes the applied loading protocol in the strong-axis direction ( $\theta_{yz}$ ) (i.e., YZ plane). Several damage states are indicated on the applied lateral loading protocol including: (a) the onset of flexural yielding, (b) the onset of local buckling, (c) beam-column axial shortening reaching 2%  $L$ , (d) out-of-plane deformations ( $\theta_x$ ) exceeding 1%  $L$ , (e) the onset of beam-column twisting (when the rotation of the beam-column cross-section about the Z-axis,  $\theta_z$ , exceeds 1 degree). Furthermore, Figs. 5 and 6 include the deduced moment-chord rotation at the column base and top. In these figures, the moment is normalized with respect to the measured plastic flexural strength  $M_p$  of the respective cross-section. The inflection point history in the strong-axis orientation is also included in Figs. 5 and 6. Selected photos of the local and global deformation profiles at discrete chord-rotations are shown for both specimens.

From Fig. 5a, the onset of flexural yielding occurred at 0.5% radians in the flanges of the Specimen C6 (W24x146,  $P/P_y=0.2$ ). Its web yielded in flexure at 1% radians. During the elastic cycles of the employed protocol the inflection point of the column remained at 0.78 $L$  from the beam-column base (see Fig. 5b) as targeted. Due to the flexible boundary condition at the beam-column top, the beam-column base exhibited inelastic deformation as seen from Figs. 5c and 5d that illustrate the deduced moment-rotation relations at the column base and top, respectively. At 1.5% radians, the specimen deteriorated in flexural strength due to the occurrence of web and flange local buckling. Local buckling in the north flange of the specimen was not visible till about 2% radians (see Fig. 5e). From Fig. 5c, the flexural strength of specimen C6 deteriorated cyclically by more than 50% compared to the maximum developed flexural strength  $M_{max}$  due to severe flange and web local buckling (see Fig. 5f). After the formation of flexural yielding and local buckling at the column base, the inflection point moved towards the beam-column base due to force redistribution within the beam-column. At the end of the test it reached to 0.43  $L$  from the beam-column base. This increased the flexural demands at the column top end. However, this

location remained essentially elastic as shown in Fig. 5d. From Fig. 5c, specimen C6 reached to a maximum flexural strength equal to its plastic flexural strength (i.e.,  $M_{max}/M_p=1.03$ ).

Based on the white paint grid shown in Fig. 5f, the center of the local buckling wave in the flanges was at  $0.7 d$  from the beam-column base. The maximum flexural strength of specimen C6 deteriorated by more than 50% at the first cycle of the 4% drift amplitude due to severe flange and web local buckling at its bottom end. The global deformation profile of the specimen at this point is shown in Fig. 5g. From this figure, it is evident that plastification mostly occurred at the column base. The test was stopped during the second excursion of the 4% drift amplitude in the strong-axis direction due to equipment limitations. At the end of the test, specimen C6 reached a maximum lateral drift ratio of 4% and 2% radians in the Y- and X-loading directions, respectively. During which, the flexural strength at the beam-column base had deteriorated by 60% and 40% in the strong and weak-axis, respectively. Beam-column twisting was fairly minimal during the test. This is confirmed from Fig. 5h that shows the global deformed shape of specimen C6 in its weak-axis direction. However, a governing failure mode that was observed on this and most of the specimens was the out-of-plane displacements of the member due to local buckling near the column base. This was equal to  $1.5\% L$  measured at  $L/4$  from the beam-column base and migrated from bottom to top along the member length. Beam-column axial shortening was slightly less than  $2.5\% L$  at the end of the test (as shown later in Fig. 8f). The unloading flexural stiffness of the specimen at its base deteriorated by 40% compared to the elastic flexural stiffness at the same location (see Fig. 5c).

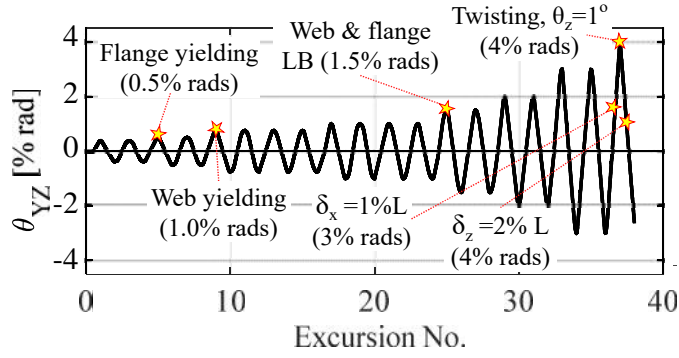
Specimen C9 utilized a more slender W24x84 cross-section. It was subjected to a bidirectional symmetric lateral loading protocol coupled with a constant compressive axial load of  $20\% P_y$ . Fig. 6a shows the damage progression of specimen C9 at its base. Flexural yielding occurred in both flanges of the specimen at the first cycle of the 0.75% drift amplitude. Local buckling occurred first in the north flange at 1.1% radians during the second cycle of the 1.5% drift amplitude. The web buckled first near the north flange of the cross-section at 1.3% radians during the same loading amplitude. The formation of flange local buckling became more evident during the first cycle of the 2% drift amplitude as shown in Fig. 6e. From this figure, the center of the local buckling wave in the flange was located at  $0.3 d$  from the beam-column base. The south flange buckled symmetrically as shown from Figs. 6f and 6g. During the first cycle of the 3% drift amplitude, the specimen lost approximately 50% of its maximum flexural strength at the beam-column base. This is shown from the deduced moment-rotation relation at the column base of specimen C9 in the strong-axis orientation (see Fig. 6c). At this loading stage, local buckling only formed at the beam-column base and not at the top as inferred from the deduced moment-rotation relation of this location, which is shown in Fig. 6d. This was the case up to about the 4% drift amplitude as shown visually from Fig. 5g that illustrates the global deformation profile of the specimen at the 1<sup>st</sup> cycle of the 4% drift amplitude. Beam-column twisting as well as the out-of-plane displacement was mostly evident near the plastic hinge closer to the beam-column base (see Fig. 6h). At this drift amplitude, the out-of-plane displacement at  $L/4$  from the beam-column base was equal to  $0.5\% L$ . From Fig. 6h, at the first cycle of the 4% drift amplitude, the beam-column out-of-plane displacement and cross-section twisting became significant due to the progression of local buckling at the beam-column base. The global geometric deformations became excessive during the first cycle of the 5% drift amplitude because of column axial shortening due to web buckling near the column base. At the end of the test, the out-of-plane

displacement  $\delta_x$  of the specimen was about 5.25%  $L$  and the twisting angle  $\theta_z$  reached  $10^\circ$ . At the end of the test, the flexural strength of the specimen in its strong-axis orientation was below zero near the beam-column base (see Fig. 6c). This occurred due to flexural strength deterioration in addition to second order effects. The flexural unloading stiffness at the beam-column base was reduced by 93% compared to the elastic one due to the occurrence of severe global instabilities. Figs. 7 and 8 illustrate the normalized moment-rotation relation and axial shortening as deduced for all ten specimens. Based on these results a number of key observations are summarized in the subsequent sections. In the same figures we have superimposed the predicted response parameters based on detailed finite element analyses briefly discussed in Section 4.5.

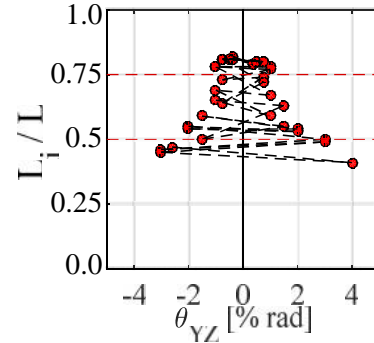
#### *4.1 Effect of local and global slenderness on the beam-column hysteretic behavior*

This section summarizes the effect of local and global slenderness on the hysteretic behavior of steel beam-columns based on the deduced moment-rotation relations for the ten specimens shown in Fig. 7. From this figure, specimens C3 (W24x146,  $P/P_y = 0.2$ ) and C7 (W24x84,  $P/P_y=0.2$ ) were subjected to a unidirectional symmetric lateral loading protocol (see Figs. 7c and 7g, respectively); specimens C5 (W W24x146,  $P/P_y=0.2$ ) and C8 (W W24x84,  $P/P_y=0.2$ ) were subjected to a unidirectional collapse-consistent loading protocol (see Figs. 7e and 7h, respectively); and specimens C6 (W24x146,  $P/P_y=0.2$ ) and C9 (W24x84,  $P/P_y=0.2$ ) were subjected to a bidirectional symmetric lateral loading protocol (see Figs. 7f and 7i, respectively). In all cases, beam-columns with  $h/t_w=33.2$  ratio deteriorated in flexural strength at about 1.5% drift ratio compared to 2% for beam-columns with  $h/t_w=45.9$ . Once web local buckling occurred, the rate of cyclic deterioration in flexural strength was much faster for beam-columns with a slender web (i.e., W24x84). This can be quantitatively seen in Fig. 7 from the post-buckling behavior of specimens that utilized a W84x84 cross-section. The post-capping slopes of these specimens were steeper compared to that observed in specimens that utilized a W24x146 cross-section and were subjected to the same lateral loading protocol. This is attributed to the progression of web local buckling of the cross-section under the presence of the constant compressive axial load. In order to better understand this issue, a comparison of the normalized beam-column axial shortening versus true chord-rotation is shown in Fig. 8 for the ten specimens. From this figure, it is evident that specimens that utilized the more slender web shortened axially faster than others that utilized a more compact one.

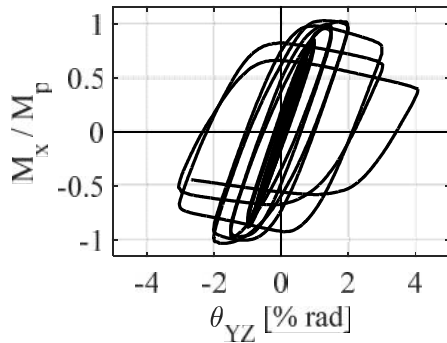
From Fig. 7i, the unloading stiffness of specimen C9 (W24x84,  $L/r_y=79$ ) deteriorated much faster after the 3% loading cycle compared to that of specimen C6 (W24x146,  $L/r_y=51$ ). The reason is that the former was more susceptible to lateral torsional buckling and the out-of-plane instability mode observed near the plastic hinge region. This issue can also be seen visually in Figs. 5h and 6h that show the out-of-plane global deformation profiles of specimens C6 and C9 at the same drift level. This issue becomes negligible when a unidirectional symmetric loading protocol is used as seen from Fig. 7g. It should be pointed out that at drift levels associated with design-basis earthquakes (i.e., 1.5% radians or less), the beam-column hysteretic behavior is not practically affected by the global and local slenderness ratios that were considered as part of the testing program.



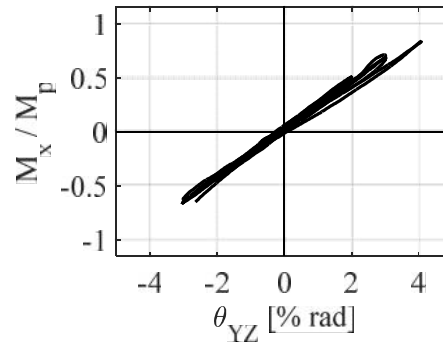
(a) Chord-rotation history in the strong-axis direction with damage states indicated



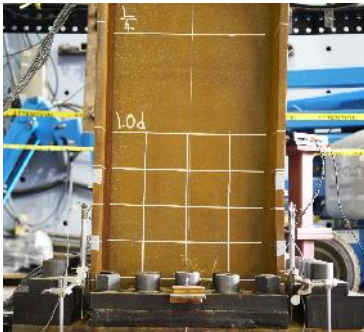
(b) Inflection point location history in the strong-axis direction



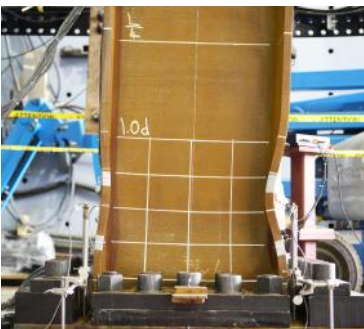
(c) Normalized moment versus true chord-rotation at beam-column base



(d) Normalized moment versus true chord-rotation at beam-column top



(e) 1<sup>st</sup> cycle, 2% drift amplitude



(f) 1<sup>st</sup> cycle, 3% drift amplitude

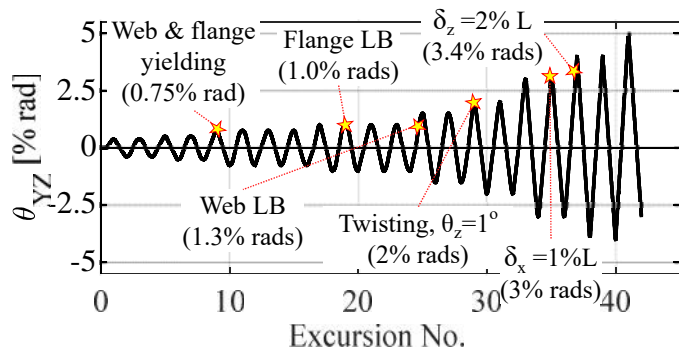


(g) 1<sup>st</sup> cycle, 4% drift amplitude

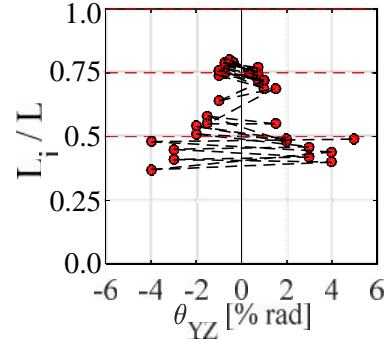


(h) 1<sup>st</sup> cycle, 4% drift amplitude

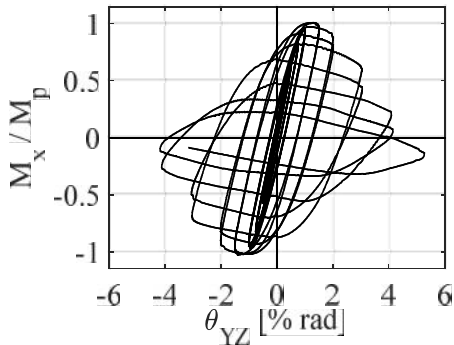
Figure 5: Damage progression for specimen C6 - W24x146 - Bidirectional symmetric lateral loading protocol



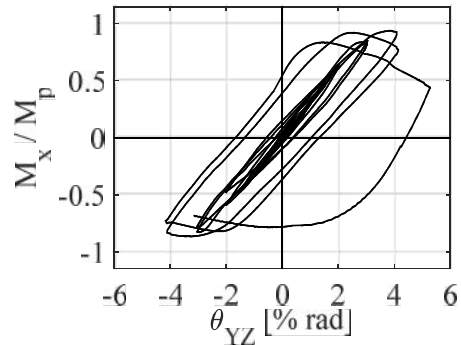
(a) Chord-rotation history in the strong-axis direction



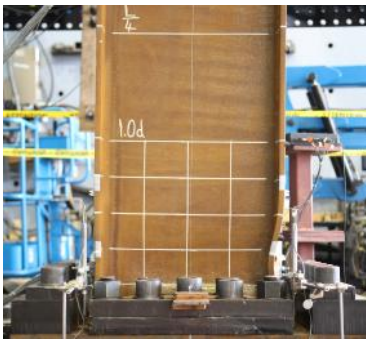
(b) Inflection point location history in the strong-axis direction



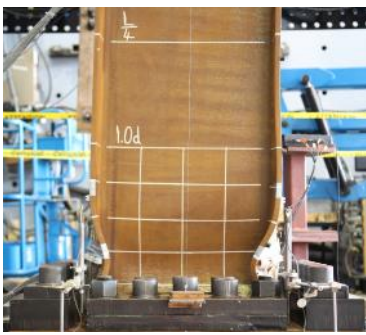
(c) Normalized moment versus true chord-rotation at beam-column base



(d) Normalized moment versus true chord-rotation at beam-column top



(e) 1<sup>st</sup> cycle, 2% drift amplitude



(f) 1<sup>st</sup> cycle, 3% drift amplitude



(g) 1<sup>st</sup> cycle, 4% drift amplitude



(h) 1<sup>st</sup> cycle, 4% drift amplitude

Figure 6: Damage progression for Specimen C9 – W24x84 - Bidirectional symmetric lateral loading protocol

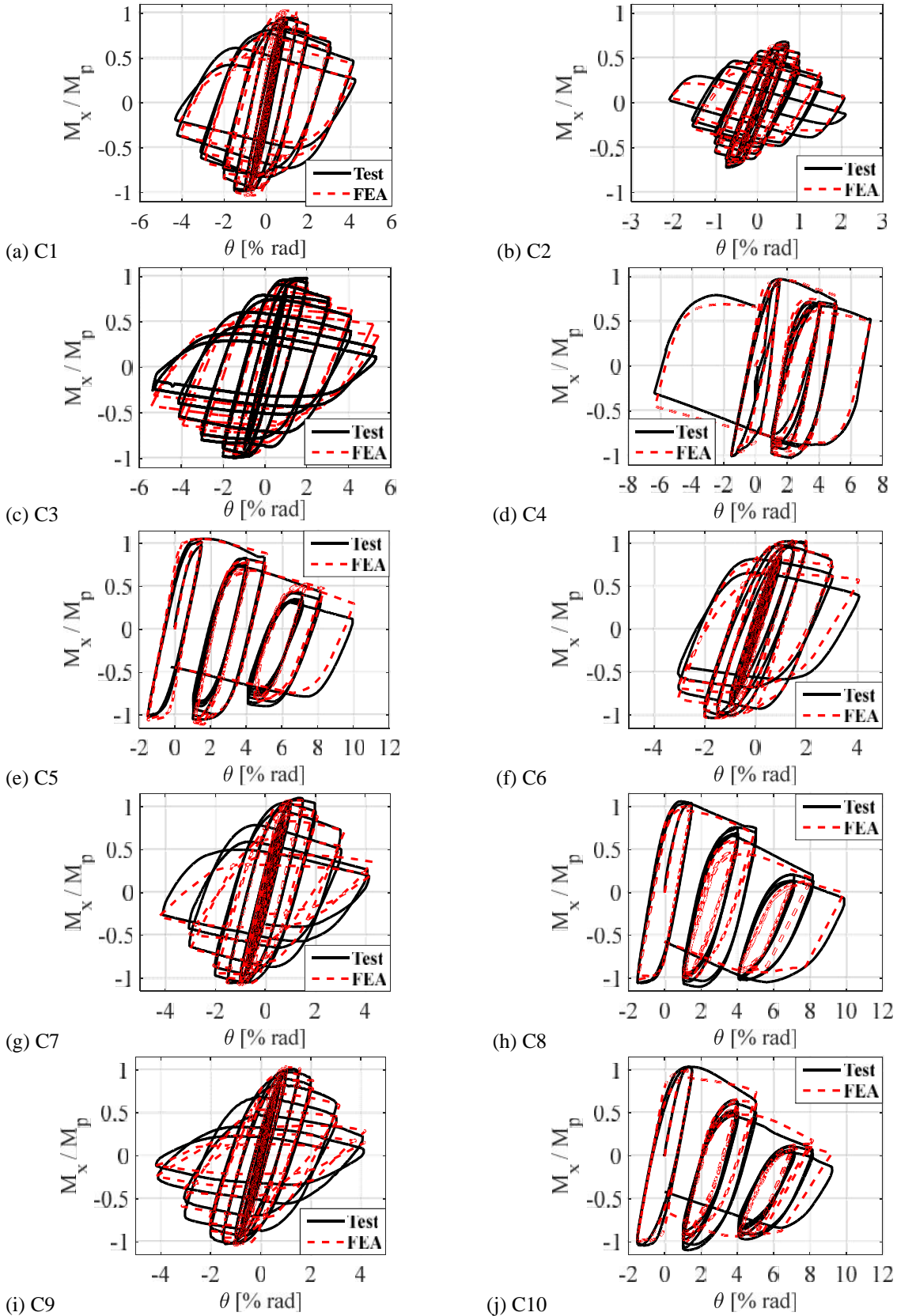


Figure 7: Normalized moment at the beam-column base versus true chord rotation

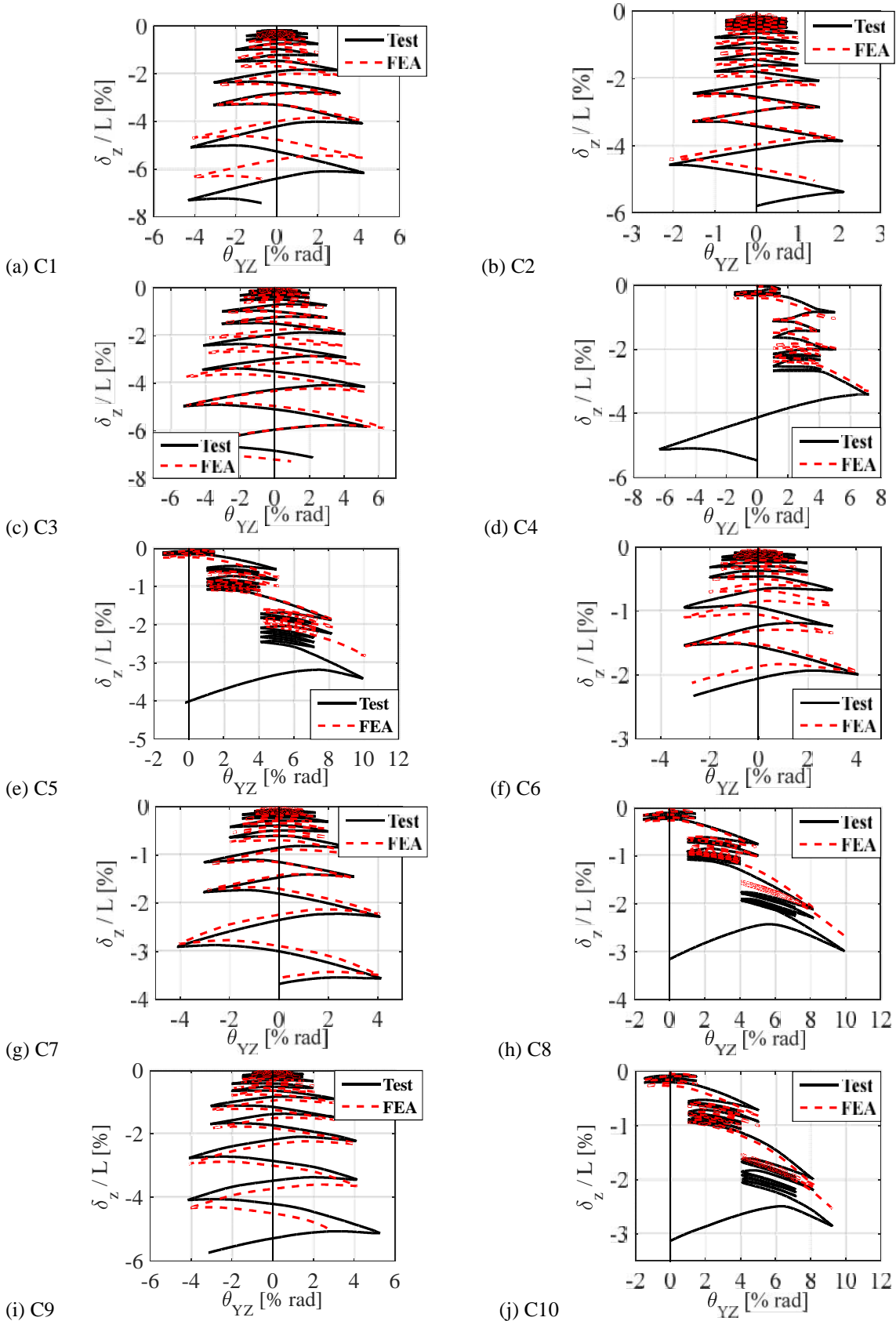


Figure 8: Normalized axial shortening versus true chord-rotation

#### 4.2 Effect of bidirectional versus unidirectional lateral loading

The testing program offers the opportunity to assess the effect of bidirectional loading on the hysteretic behavior of nominally identical specimens that were also subjected to a unidirectional lateral loading protocol. To the best of the author's knowledge this has never been addressed in prior experimental studies. Three pairs of specimens can be compared for this purpose; specimens C3 (W24x146, Unidirectional) and C6 (W24x146, Bidirectional) that were subjected to symmetric lateral loading protocols; specimens C7 (W24x84, Unidirectional) and C9 (W24x84, Bidirectional) that were subjected to symmetric lateral loading protocols; and specimens C8 (W24x84, Unidirectional) and C10 (W24x84, Bidirectional) that were subjected to collapse-consistent lateral loading protocols. Each pair involves specimens with the same cross-section and boundary conditions. The applied axial compressive load was kept the same in all cases (i.e.,  $P/P_y = 0.20$ ). From Fig. 7, the plastic deformation capacity of a beam-column is not sensitive to bidirectional lateral loading. This observation holds true regardless of the cross-section and type of lateral loading (i.e., symmetric or collapse-consistent). Same observations hold true in terms of the beam-column axial shortening as shown in Fig. 8. In that respect, if the objective is to construct a first-cycle envelope curve for beam-columns for the nonlinear evaluation of steel moment-resisting frames under seismic loading this can be done with experimental data based on unidirectional loading protocols.

By comparing Figs. 7c and 7f; Figs. 7g and 7i; and Figs. 7h and 7j, it is shown that for story drift ratios larger than 3% radians, the rate of cyclic deterioration in flexural strength of a beam-column was slightly larger under bidirectional lateral loading compared to that from unidirectional lateral loading. This is attributed to the additional flexural demands in the weak-axis direction of the beam-column cross section. This effect is practically negligible if the cyclic behavior is evaluated based on the first-cycle envelope curves. From Figs. 7g and 7i as well as Figs. 7h and 7j, for story drift ratios larger than 3% radians the unloading stiffness of a beam-column that was subjected to bidirectional symmetric lateral loading deteriorated much more compared to that from unidirectional lateral loading. This is attributed to the magnitude of out-of-plane deformations near the plastic hinge region at the beam-column base as well as the deformations due to lateral torsional buckling along the height of the cross-section when a beam-column experienced bidirectional lateral loading.

#### 4.3 Effect of the lateral loading protocol type

The testing program also highlights the effect of the lateral loading protocol type on the beam-column hysteretic behavior. This is a critical issue for the calibration of component models to simulate the cyclic and in-cycle deterioration in flexural strength and stiffness of steel beam-columns in steel MRFs. These models are typically considered for simulating the earthquake-induced collapse of steel frame buildings. Based on Fig. 7, specimens subjected to a collapse-consistent lateral loading protocol had at least double plastic deformation capacity compared to nominally identical specimens that were subjected to a symmetric cyclic lateral loading protocol. From the same figures, at the second cycle of the 4% drift amplitude, specimens subjected to a symmetric lateral loading protocol lost more-or-less their flexural strength. However, specimens subjected to a collapse-consistent lateral loading protocol maintained at least 80% of their maximum flexural strength at the same drift amplitude. Same observations hold true in terms of

the measured beam-column axial shortening based on the two lateral loading protocols as shown in Fig. 8. Specimens that experienced a collapse-consistent lateral loading protocol shortened on average by 1%  $L$  at a 4% drift amplitude. This was at least 5 to 6 times less than the measured axial shortening in specimens subjected to a symmetric lateral loading protocol. All the aforementioned issues are attributed to the large number of inelastic cycles that a specimen experiences when it is subjected to a symmetric lateral loading protocol. However, prior to structural collapse, a steel beam-column as part of steel MRF subjected to an ordinary ground motion would typically experience very few inelastic cycles followed by large monotonic pushes in one loading direction. This is consistent with results from shake table collapse experiments on steel frame buildings (Lignos et al. 2011; Lignos et al. 2013). From Fig. 7, prior to the onset of flexural strength deterioration (i.e., drift range of 2% radians or less), it is clear that the employed lateral loading protocol did not affect the beam-column hysteretic behavior. Therefore, for life-safety the choice of the lateral loading protocol to characterize the beam-column hysteretic behavior is not relevant. However, test data from specimens subjected to symmetric lateral loading protocols appear to be over-conservative for characterizing the hysteretic behavior of structural steel components at large displacements associated with structural collapse. This agrees with earlier findings by Suzuki and Lignos (2015) after conducting a large-scale testing program on cantilever steel beam-columns that utilized slender but seismically compact W14 cross-sections. In that sense, the use of the first-cycle envelope curve is not recommended given its sensitivity to the lateral loading history. This also agrees with studies summarized in FEMA 440A (FEMA 2009). In that respect, for collapse-related studies the use of the monotonic backbone is recommended for modeling the load-deformation envelope relation of a steel beam-column. For calibration of component models that are able to trace the cyclic deterioration in flexural strength of steel beam-columns the use of the collapse-consistent loading protocol is recommended (Suzuki and Lignos 2015).

#### *4.4 Lateral bracing force demands for beam-columns*

One of the main aspects of the 6-DOF test setup is the ability to measure the out-of-plane forces acting at the top end of a specimen under a unidirectional test. These forces could be used for the design of lateral bracing of steel beam-columns. To the best of the author's knowledge this has never been considered in prior experimental studies. Figs. 9a and 9b show the history of the out-of-plane force,  $F_x$ , normalized with respect to the measured axial yield strength of the respective specimen,  $P_y$ , for specimens C5 (W24x146,  $P/P_y=0.20$ ) and C8 (W24x84,  $P/P_y=0.20$ ) subjected to unidirectional lateral loading, respectively. Based on these figures, specimen C5 experienced a maximum out-of-plane force equal to 1.7%  $P_y$  while specimen C8 that utilized a more slender cross-section experienced a maximum out-of-plane force equal to 0.8%  $P_y$ . The fact that specimen C8 experienced fairly low out-of-plane forces at its top end is attributed to its relatively low weak-axis moment-of-inertia, radius-of-gyration, and torsional constant of the compared to the specimen C5. These properties are related to the torsional resistance of a cross-section.

For the stability design of steel beam-columns, the steel specifications in Canada and the U.S. (CSA 2009; AISC 2010b) provide design formulas for the expected axial force required for the bracing member in the direction perpendicular to the beam-column strong-axis. Based on Section 27.2.6 of the CSA (2009), for the seismic design of Ductile (Type D) steel MRFs, columns and beam-to-column joints shall be braced by members proportioned in accordance with Clause 9.2

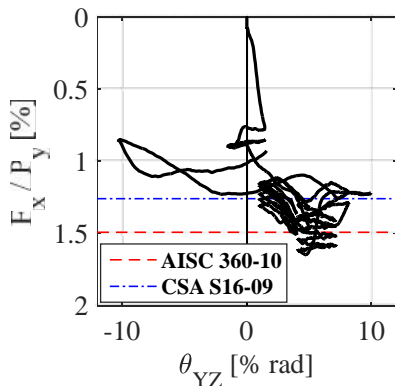
of the same document. Clause 9.2.5 specifies a lateral brace axial strength ( $P_b$ ) equal to at least 2% of the factored compressive force  $C_f$  of the element being braced laterally, as given by Eq. 1,

$$P_b = 0.02 C_f = 0.02(1.1 R_y f_{yn} A_{comp}) \quad (1)$$

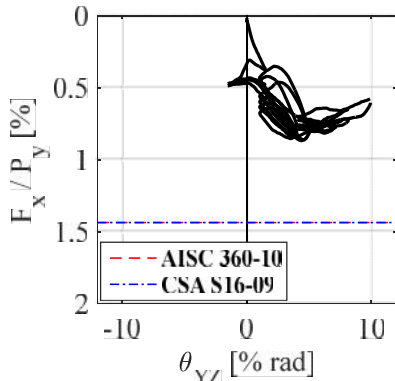
in which,  $R_y$  is a factor applied to estimate the probable yield stress (taken as 1.1),  $F_{yn}$  is the nominal yield stress of the steel material, and  $A_{comp}$ , is the cross-sectional area in compression. Similarly, based on Section 6.4 of the ANSI/AISC 360-10 (AISC 2010b), for the lateral bracing of beam-columns, the required strength for the nodal brace axial force ( $P_{rb}$ ) shall be determined as the sum of the beam bracing axial force and column bracing axial force as given by Eq. 2,

$$P_{rb} = 0.01 P_r + 0.02 M_r C_d / h_o \quad (2)$$

in which,  $P_r$  and  $M_r$  are the required axial and flexural strength of the beam-column, respectively,  $h_o$  is the distance between flange centroids, and  $C_d = 2.0$  for braces closest to the column inflection point. Note that the “nodal brace” design force discussed here is more conservative compared to the lower “relative brace” design force specified in AISC (2010b).



(a) Specimen C5 – W24x146-CPS-20-Unidirectional



(b) Specimen C8 – W24x84-CPS-20-Unidirectional



(c) Specimen C5 – W24x146-CPS-20-Unidirectional, at the first 8% drift amplitude



(d) Specimen C8 – W24x84-CPS-20-Unidirectional, at the first 8% drift amplitude

Figure 9: Normalized out-of-plane force versus true-chord-rotation in the strong-axis direction (*left*) and out-of-plane global deformation profile (*right*)

The lateral brace design axial force for each specimen is calculated as per CSA (2009) and AISC (2010b) based on Eqs. 1 and 2. The computed values are superimposed in Fig. 9. Note that for the calculation of  $P_b$  (CSA 2009),  $A_{comp}$  is calculated assuming that 65% of the cross-section depth is under compression when subjected to 20%  $P_y$ . This is based on a stress distribution given that flexural yielding reached the extreme fibers of the cross-section. For the calculation of  $P_{rb}$  (AISC 2010b),  $P_r$  is assumed to be equal to the axial load ratio applied to the corresponding specimen (i.e.,  $P_r = P/P_y$ ) and  $M_r$  is assumed to be equal to the reduced plastic flexural strength [i.e.,  $M_r = M_p (1 - P/P_y)$ ]. Based on Fig. 9a, the maximum out-of-plane axial force demand for specimen C5 seem to be adequate for story drift ratios up to 2% radians that are associated with design-basis earthquakes. However, at larger lateral drift demands associated with seismic events with low-probability of occurrence, the out-of-plane axial force demands exceeded the lateral bracing design axial force specified by both the CSA (2009) and AISC (2010b) provisions by 15% and 35%, respectively. On the other hand, the lateral bracing design axial force seems to be fairly conservative for specimens that utilized the more slender W24x84 cross-section regardless of the lateral drift demands. These observations suggest the need to re-visit the seismic design formulas for the lateral brace design axial force for beam-columns in steel MRFs. The authors are currently working on this issue.

#### *4.5 Corroborating continuum finite-element analyses*

Although the beam-column test data discussed previously provide valuable insights into the beam-column hysteretic behavior, it is not easy to generalize the experimental findings discussed in Sections 4.1 to 4.4 due to the limited range of parameters covered in the experimental program. Thus, analytical simulations are also conducted in parallel with the experimental program. A continuum finite element approach is employed for this purpose that is able to simulate the global and local geometric effects observed in deep and slender wide-flange beam-columns. The effect of material nonlinearity and residual stresses due to hot rolling is also captured. All the aspects of the finite element modeling approach are summarized in great detail in Elkady and Lignos (2015a). Figs. 7 and 8 provide comparisons between the simulated and measured hysteretic behavior of all ten specimens in terms of moment-rotation and axial shortening-rotation relations, respectively. From these comparisons, it is evident that the FE modeling approach is able to simulate complex-deteriorating modes associated with the dynamic stability of steel wide-flange beam-columns. The authors are currently using these models to generalize the findings from the beam-column tests through a corroborating parametric study with the aim to further refine the current seismic design practice for wide-flange beam-columns in steel moment-resisting frames. Another goal of this study is to develop nonlinear modeling recommendations for steel beam-columns for the assessment of new and existing steel frame buildings subjected to earthquake loading.

### **5. Conclusions**

This paper discusses the findings from a full-scale testing program on deep and slender steel wide-flange beam-columns. The testing program involved ten specimens that are typically seen in interior first-story columns of steel special moment frames (SMFs); six specimens utilized a W24x146 cross-section. The rest utilized a W24x84 cross-section. The specimens were tested under both bidirectional and unidirectional lateral loading protocols representative of design-basis and collapse consistent seismic events. Eight specimens were tested with flexible boundary

conditions at the beam-column top to represent the flexibility of a beam-to-column joint. The main observations from the experimental program are summarized as follows:

- Beam-columns utilizing a W24x84 cross-section experience higher rates of cyclic deterioration in flexural strength and stiffness compared to that from beam-columns utilizing a W24x146 cross-section. This is attributed to the early occurrence of web and flange local buckling.
- At a given chord-rotation, the beam-columns with a W24x84 experience an axial shortening that is about 10% to 20% higher than that of the W24x146 beam-columns. This issue is mostly attributed to the early onset of web local buckling.
- Due to column axial shortening a common failure mode that was observed in all the specimens was the out-of-plane instability near the plastic hinge region at the column base. This instability migrated from bottom to top along the member length.
- Beam-columns subjected to a collapse-consistent lateral loading protocol achieved a plastic deformation capacity that was 1.5 to 2 times larger than that of nominally identical beam-columns subjected to a symmetric lateral loading protocol. This is attributed to the excessive number of inelastic cycles that the latter imposes compared to few inelastic cycles followed by a large monotonic push in on loading direction from the former.
- Beam-columns subjected to a collapse-consistent lateral loading protocol shortened on average by 1%  $L$  at a 4% drift amplitude, which was 5 to 6 times less than that measured in nominally identical beam-columns subjected to a symmetric lateral loading protocol.
- Beam-columns subjected to bidirectional lateral loading experienced slightly larger levels of cyclic deterioration in flexural strength compared to those subjected to unidirectional lateral loading. This is attributed to the additional flexural demands and P-Delta forces in the weak-axis direction of the beam-column.
- The effect of the bidirectional lateral loading protocol on flexural stiffness and out-of-plane instability was more evident in beam-columns that utilized a W24x84 cross-section. This was attributed to the larger global slenderness ratio ( $L/r_y \sim 79$ ) that these specimens had compared to those with a W24x146 cross-section ( $L/r_y \sim 50$ ).
- The lateral bracing design axial force per CSA (2009) and AISC (2010b) seems to be adequate for beam-columns that utilize a W24x146 cross-section ( $h/t_w < 33$  and  $L/r_y < 52$ ) and experience lateral drift ratios 2% or less. For beam-columns that experienced drift ratios larger than 4% radians, CSA (2009) and AISC (2010b) specifications underestimate the lateral bracing design axial force. On the other hand, the lateral bracing axial force design requirements per CSA (2009) and AISC (2010b) seem to be fairly conservative for beam-columns with  $h/t_w \sim 47$  and  $L/r_y \sim 80$ .

The authors are currently using continuum finite element models validated with data from the experimental program discussed in this paper to generalize the findings from the beam-column tests through a corroborating parametric study with the aim to further refine the current seismic design practice for wide-flange beam-columns in steel moment-resisting frames.

### **Acknowledgments**

This study is based on work supported by the National Science and Engineering Research Council of Canada (NSERC) under the Discovery Grant Program. The Steel Structures Education Foundation (SSEF) also provided funding for the testing program. The financial support is gratefully acknowledged. The ADF Corporation Inc. donated the material and

fabrication for four of the specimens. The authors would like to sincerely thank Prof. Robert Tremblay, École Polytechnique de Montréal (EPM), for providing the opportunity to use the unique 6-DOF test setup and resources at EPM. The authors sincerely thank the technical staff at the EPM structures laboratory for their invaluable assistance during the testing program. Any opinions, findings, and conclusions or recommendations expressed in this paper are those of the authors and do not necessarily reflect the views of sponsors.

## References

- AISC (2010a). "Seismic Provisions for Structural Steel Buildings", ANSI/AISC 341-10. American Institute for Steel Construction, Chicago, IL.
- AISC (2010b). "Specification for Structural Steel Buildings", ANSI/AISC 360-10. American Institute for Steel Construction, Chicago, IL.
- ASCE (2010). "Minimum Design Loads for Buildings and Other Structures", ASCE/SEI 7-10. American Society of Civil Engineers, Reston, VA.
- ASTM (2014). "Standard Specification for General Requirements for Rolled Structural Steel Bars, Plates, Shapes, and Sheet Piling", ASTM A6/A6M-14. American Society for Testing and Materials, West Conshohocken, PA.
- Clark, P., Frank, K., Krawinkler, H. and Shaw, R. (1997). "Protocol for Fabrication, Inspection, Testing, and Documentation of Beam-Column Connection Tests and Other Experimental Specimens", Report No. SAC/BD-97. SAC Joint Venture.
- CSA (2009) Design of Steel Structures. Canadian Standards Association, Mississauga, Canada
- Elkady, A. and Lignos, D. G. (2012). "Dynamic Stability of Deep Slender Steel Columns as Part of Special MRFs Designed in Seismic Regions: Finite Element Modeling". *Proceedings of First International Conference on Performance-Based and Life-Cycle Structural Engineering (PLSE)*, Hong Kong, China, December 5-7, 2012.
- Elkady, A. and Lignos, D. G. (2013). "Collapse Assessment Special Steel Moment Resisting Frames Designed with Deep Members". *Proceedings of Vienna Congress on Recent Advances in Earthquake Engineering and Structural Dynamics (VEESD)*, Vienna, Austria, August 28-30, 2013.
- Elkady, A. and Lignos, D. G. (2014). "Modeling of the Composite Action in Fully Restrained Beam-to-Column Connections: Implications in the Seismic Design and Collapse Capacity of Steel Special Moment Frames". *Earthquake Engineering & Structural Dynamic*; 43 (13) 1935-1954. DOI: 10.1002/eqe.2430.
- Elkady, A. and Lignos, D. G. (2015a). "Analytical Investigation of the Cyclic Behavior and Plastic Hinge Formation in Deep Wide-Flange Steel Beam-Columns". *Bulletin of Earthquake Engineering*; 13 (4) 1097-1118. DOI: 10.1007/s10518-014-9640-y.
- Elkady, A. and Lignos, D. G. (2015b). "Effect of Gravity Framing on the Overstrength and Collapse Capacity of Steel Frame Buildings with Perimeter Special Moment Frames". *Earthquake Engineering & Structural Dynamic*; 44 (8) 1289-1307. DOI: 10.1002/eqe.2519.
- FEMA (2000). "State of the Art Report on Connection Performance", Report FEMA-355D. Federal Emergency Management Agency, Washington, DC.
- FEMA (2009). "Effects of Strength and Stiffness Degradation on the Seismic Response of Structural Systems", Report FEMA-P440A. Federal Emergency Management Agency, Washington, DC.
- Fogarty, J. and El-Tawil, S. (2015). "Collapse Resistance of Steel Columns under Combined Axial and Lateral Loading". *Journal of Structural Engineering*. DOI:10.1061/(ASCE)ST.1943-541X.0001350.
- Lignos, D. G. and Krawinkler, H. (2011). "Deterioration Modeling of Steel Components in Support of Collapse Prediction of Steel Moment Frames under Earthquake Loading". *Journal of Structural Engineering*; 137 (11) 1291-1302. DOI: 10.1061/(ASCE)ST.1943-541X.0000376.
- Lignos, D. G., Krawinkler, H. and Whittaker, A. S. (2011). "Prediction and Validation of Sidesway Collapse of Two Scale Models of a 4-Story Steel Moment Frame". *Earthquake Engineering & Structural Dynamics*; 40 (7) 807-825. DOI: 10.1002/eqe.1061.
- Lignos, D. G., Hikino, T., Matsuoka, Y. and Nakashima, M. (2013). "Collapse Assessment of Steel Moment Frames Based on E-Defense Full-Scale Shake Table Collapse Tests". *Journal of Structural Engineering*; 139 (1) 120-132. DOI: 10.1061/(ASCE)ST.1943-541X.0000608.
- Lignos, D. G. and Krawinkler, H. (2013). "Development and Utilization of Structural Component Databases for Performance-Based Earthquake Engineering". *Journal of Structural Engineering*; 139 (8) 1382-1394. DOI: 10.1061/(ASCE)ST.1943-541X.0000646.

- MacRae, G. A., Carr, A. J. and Walpole, W. R. (1990). "The Seismic Response of Steel Frames", Report No. 90-6. Department of Civil Engineering, University of Canterbury, New Zealand.
- Newell, J. D. and Uang, C.-M. (2006). "Cyclic Behavior of Steel Columns with Combined High Axial Load and Drift Demand", Report No. SSRP-06/22. Department of Structural Engineering, University of California, San Diego.
- NIST (2010). "Research Plan for the Study of Seismic Behaviour and Design of Deep Slender Wide Flange Structural Steel Beam-Column Members", NIST GCR 11-917-13. NEHRP consultants Joint Venture.
- Suzuki, Y. and Lignos, D. G. (2014). "Development of Loading Protocols for Experimental Testing of Steel Columns Subjected to Combined High Axial Load and Lateral Drift Demands Near Collapse". *Proceedings of 10th National Conference on Earthquake Engineering (10th NCEE)*, Anchorage, Alaska, USA, July 21-25, 2014.
- Suzuki, Y. and Lignos, D. G. (2015). "Large Scale Collapse Experiments of Wide Flange Steel Beam-Columns". *Proceedings of The 8th International Conference on Behavior of Steel Structures in Seismic Areas (STESSA)*, Shanghai, China, July 1-3, 2015.
- Uang, C.-M., Ozkula, G. and Harris, J. (2015). "Observations from Cyclic Tests on Deep, Slender Wide-Flange Structural Steel Beam-Column Members". Paper presented at the The Annual Stability Conference, Structural Stability Research Council (SSRC), Nashville, Tennessee, USA, March 24-27, 2015.
- Zhang, X. and Ricles, J. M. (2006). "Seismic Behavior of Reduced Beam Section Moment Connections to Deep Columns". *Journal of Structural Engineering*; 132 (3) 358-367